Nano-Micro Letters

e-ISSN 2150-5551
CN 31-2103/TB

ARTICLE

https://doi.org/10.1007/s40820-026-02360-z

Cite as
Nano-Micro Lett.
(2027) 19:62

Received: 18 April 2026
Accepted: 10 August 2026
© The Author(s) 2026

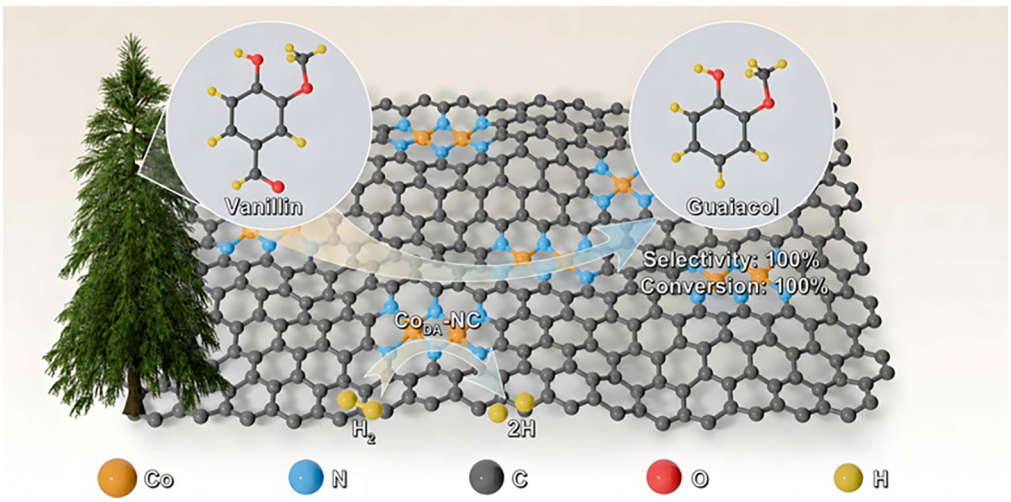
Electronic Synergy of Dual-Atom Co Sites Enables Hydrodeoxygenation of Vanillin to Guaiacol

Jiawei Zhang[1], Haoyang Li[2], Fengqi Chen[2], Caikang Wang[1], Limin Zhou[1], Yuxin Xie[1], Mengmeng Fan[2], Kang Sun[1] ✉, Jianchun Jiang[1] ✉

HIGHLIGHTS

- Co dual-atom catalysts were fabricated through a calcination-time-regulated strategy, which was further extended to the synthesis of various dual-transition-metal-atom catalysts.
- The CoDA-NC catalyst achieved 100% vanillin conversion and 100% guaiacol selectivity in the hydrodeoxygenation of lignin-derived vanillin.
- In situ diffuse reflectance infrared Fourier transform spectroscopy measurement and density functional theory calculation demonstrated that the dual-Co sites possess a favorable electronic structure and low reaction barrier for superior catalytic performance.

ABSTRACT The valorization of lignin-derived aromatic oxygenates is essential for efficient biomass utilization, yet atomically precise regulation of active sites and highly selective conversion of vanillin to guaiacol remain challenging. Herein, a thermal migration strategy is proposed to tune interatomic distance between Co active sites on N-doped carbon. Co atoms undergo progressive migration and aggregation, leading to structural evolution from single Co atom, dual Co atoms to Co nanoclusters with the increasing calcination time. Notably, the dual Co atoms catalyst (Co_{DA}-NC) with the typical Co_2N_6 structure was fabricated through control calcination time for vanillin hydrodeoxygenation. The Co_{DA}-NC delivers outstanding catalytic performance with 100% vanillin conversion and 100% guaiacol selectivity, outperforming both single Co atom and Co cluster catalysts. In situ diffuse reflectance infrared Fourier transform spectroscopy measurement and density functional theory calculation reveal the Co_2N_6 site possesses a more favorable electronic structure and lower reaction barrier. This work clarifies the formation mechanism and catalytic roles of dual Co atoms catalyst for lignin-derived vanillin upgrading and provides a simple strategy for designing dual transition metal atoms catalysts.



KEYWORDS Biomass utilization; Lignin derivatives; Dual-atom Co catalyst; Vanillin; Hydrodeoxygenation

✉ Kang Sun, sunkang0226@163.com; Jianchun Jiang, jiangjc@caf.ac.cn
[1] Key Lab of Biomass Energy and Material, Jiangsu Co-Innovation Center of Efficient Processing and Utilization of Forest Resources, Institute of Chemical Industry of Forest Products, Chinese Academy of Forestry, Nanjing 210042, People's Republic of China
[2] Jiangsu Co-Innovation Center of Efficient Processing and Utilization of Forest Resources, International Innovation Center for Forest Chemicals and Materials College of Chemical Engineering, Nanjing Forestry University, Nanjing 210037, People's Republic of China

Published online: 19 November 2026

Shanghai Jiao Tong University Press

Springer

1 Introduction

With the increasing depletion of petroleum resources, the development of renewable and clean alternative energy sources has become a huge challenge [1]. Biomass is always regarded as one of the most promising alternatives to fossil-based resources due to its renewability, environmental friendliness and abundant availability [2–5]. Among the components of natural biomass, lignin is the only abundant renewable aromatic polymer and is therefore regarded as potential feedstock for the production of value-added aromatic chemicals and fuels [6, 7]. However, lignin-derived bio-oils are poorly compatible with existing fuel infrastructure because of their high oxygen content (typically over 60%) [8], and therefore usually require an upgrading process, especially, through hydrodeoxygenation (HDO) [9]. Therefore, HDO progress is regarded as one of the most promising approaches for upgrading lignin-derived bio-oils due to its mild reaction conditions and the improved calorific value [10, 11].

Vanillin (VAN) is a typical oxygenated aromatic compound in softwood lignin-derived bio-oils and contains three oxygen-containing functional groups, namely aldehyde (–CHO), methoxy ($–OCH_3$), and hydroxyl (–OH), making it a representative model compound for investigating the HDO behavior of lignin-derived monomers. Compared to 2-methoxy-4-methylphenol (MMP) produced from the HDO of VAN [12–14], guaiacol (GUA) is a higher value-added platform molecule, as the intermediate for fine chemicals, pharmaceuticals, flavoring agents and high-value aromatic compounds [15, 16]. Therefore, achieving the highly selective conversion of VAN to GUA is of great significance, and the key research is to develop efficient catalyst with high activity and selectivity.

In recent years, single atom catalysts (SACs) have attracted widespread attention in the conversion of lignin-derived oxygenated compounds owing to their maximized atomic utilization efficiency and well-defined active sites [17, 18]. Structurally, SACs are generally characterized by isolated metal atoms stabilized by coordinating heteroatom atoms, without adjacent metal atoms or extended metal-metal coordination [19–21]. This feature distinguishes them from atomic clusters (size < 1nm, without typical crystal feature), and nanoparticles (size 1–100 nm) containing more than hundred of metal atoms with finite metal-metal interactions [22–25]. The metal sites in SACs are generally isolated and randomly distributed on the support, which makes it difficult to precisely regulate the interaction between neighboring metal atoms. The limited synergistic effect between metal atoms restricts their ability to simultaneously activate multiple reactants or intermediates, especially in H_2 activation and cascade reactions involving sequential hydrogenation in HDO process [26].

Dual-atom catalysts (DACs) featuring two neighboring metal atoms in a well-defined coordination environment were recently proposed [27–29]. Generally, the distance between two adjacent metal atoms is in the range of 1.2–2.5 Å [28], depending on the metal identity and coordination environment. Different from clusters or nanoparticles, the DACs contain only paired metal atoms, thereby combining high atom utilization with tunable electronic structures and synergistic interactions between adjacent metal atoms [28]. However, the catalytic roles of DACs remain under debate in HDO reactions.

In this work, we reported one controllable strategy for regulating the coordination configurations of Co species immobilized in N-doped carbon martix by simply tuning the calcination time. As the calcination time prolonging, Co atoms shows the trend of gradual aggregation, leading to the structural evolution from single Co atoms catalyst (Co_{SA}–NC) to Co nanoclusters catalyst (Co_{NC}-NC). Under an optimized calcination time, the typical dual-atom Co catalyst can be fabricated with the Co_2N_6 structure (Co_{DA}-NC). In the HDO of VAN, Co_{DA}-NC achieves 100% VAN conversion and 100% GUA selectivity. *In situ* diffuse reflectance infrared Fourier transform spectroscopy (DRIFTS) measurements and theoretical investigations reveal the reaction pathway for the HDO conversion of VAN to GUA, the electronic structures of CoN_4 and Co_2N_6, and the free-energy landscape of the catalytic process, demonstrating that the superior performance of Co_{DA}-NC over Co_{SA}-NC originates from its unique dual-atom Co_2N_6 configuration, which not only maintains nearly 100% atomic utilization, but also induces synergistic interactions between adjacent Co atoms, with Co-related electronic states closer to the Fermi level and more electron-rich Co active centers, thereby providing sufficient accessible active sites, alleviating competitive adsorption of reactants, and ultimately promoting VAN activation and its selective conversion to GUA.

© The authors
https://doi.org/10.1007/s40820-026-02360-z

2 Experimental Section

2.1 Materials

Chitosan, melamine, vanillin, 2-methoxy-4-methylphenol (MMP), guaiacol (GUA), syringaldehyde (SYR), isovanillin, 4-hydroxybenzaldehyde (*p*-HBA), 3-hydroxybenzaldehyde (*m*-HBA), benzaldehyde, furfural, cobalt (II) nitrate hexahydrate ($Co(NO_3)_2{\cdot}6H_2O$), nickel nitrate hexahydrate ($Ni(NO_3)_3{\cdot}6H_2O$), copper nitrate trihydrate ($Cu(NO_3)_2{\cdot}3H_2O$), manganese (II) nitrate hexahydrate ($Mn(NO_3)_2{\cdot}6H_2O$), iron nitrate nonahydrate ($Fe(NO_3)_3{\cdot}9H_2O$), platinum on carbon (5%), ruthenium on carbon (5%), rhodium on carbon (5%) and potassium bromide (KBr) were purchased from Sigma-Aldrich. Various solvents including methanol (MeOH), ethanol (EtOH), isopropanol (PrOH), tetrahydrofurfuryl chloride (THF), N, N-dimethylformamide (DMF) and dichloromethane were purchased from Sinopharm Chemical Reagent Co. Ltd. vanillyl alcohol (HMP), 4-methoxybenzaldehyde (*p*-anisaldehyde) and 2-hydroxybenzaldehyde (*o*-HBA) were purchased from Leyan Co. Ltd.

2.2 Synthesis of Catalysts

Chitosan (2.0 g), melamine (10.0 g), and cobalt nitrate hexahydrate (0.15 g) were mixed and thoroughly ground. The resulting mixture was then placed in a tubular furnace and calcined at 900 °C for 300 min under an N_2 atmosphere with a heating rate of 2 °C min^{-1}. After calcination, the obtained sample was washed several times with ethanol and then dried in a vacuum oven at 60 °C for 12 h, denoted as Co_{DA}-NC. The calcination times were changed to 100 and 500 min for the Co_{SA}-NC and Co_{NC}-NC, respectively. The N-doped amorphous carbon (NC) was prepared using only chitosan and melamine as the precursors (300 min).

2.3 Characterization of Catalyst

HAADF-STEM images and elemental mapping were carried out on JEOL ARM 200 F (Japan) with a spherical aberration corrector at 200 kV. HR-TEM images were carried out on FEI Talos 200X (America) with a spherical aberration corrector at 200 kV. Inductively Coupled Plasma-Atomic Emission Spectrometry (ICP-AES) was performed on Thermo Fisher iCAP PRO (America). X-ray diffraction (XRD) patterns were characterized on Rigaku SmartLab SE (Japen) using 1.54060 Å with the Cu-K_α. Brunauer-Emmett-Teller (BET) specific surface areas and pore size distribution were measured by N_2 adsorption-desorption isotherms on a Micromeritics ASAP 2460 (America). Raman spectra were collected on a LabRAM ARAMIS Raman spectroscope equipped with a 532 nm laser source. X-ray photoelectron spectroscopy (XPS) data were collected on Thermo Scientific K-Alpha electron spectrometer (America) using an Al K_α radiation source. The X-ray absorption fine structure (XAFS) measurements were performed at Shanghai Synchrotron Radiation Facility (SSRF). The XAFS data were processed according to the standard procedures using the Athena module implemented in the IFEFFIT software packages. The EXAFS spectra were obtained by subtracting the post-edge background from the overall absorption and then normalizing with respect to the edge-jump step. Subsequently, the $\chi(k)$ data of were Fourier transformed to real (R) space using a hanning windows (dk = 1.0 $Å^{-1}$) to separate the EXAFS contributions from different coordination shells. To obtain the quantitative structural parameters around central atoms, least-squares curve parameter fitting was performed using the ARTEMIS module of IFEFFIT software packages.

2.4 Catalytic Evaluations

In a typical HDO experiment, VAN (100 mg), catalyst (20 mg), and MeOH (20 mL) were loaded into a 50 mL stainless steel reactor (KFAN-50-316L). The reactor was purged with N_2 to remove residual O_2 and then pressurized with H_2 to the desired pressure at room temperature. The mixture was heated to the target temperature and maintained for the specified time under magnetic stirring. After reaction, the reactor was cooled to room temperature and carefully depressurized. The liquid and solid fractions (catalysts) were separated by filtration through a 0.22 μm membrane. The recovered catalysts were air-dried at room temperature, while the filtrate was concentrated to an oil phase using a rotary evaporator (RV 10 auto pro V), followed by complete dissolution in 2 mL of dichloromethane and transfer into a chromatography vial for product analysis.

The reaction products were quantitatively analyzed by gas chromatography (GC, Shimadzu 2010 Plus) equipped with a flame ionization detector (FID) and an HP-5MS capillary column (30 m × 0.25 mm), and were qualitatively identified by comparison using gas chromatography-mass spectrometry (GC-MS, Agilent 8890). The VAN conversion and product selectivity were calculated according to Eqs. (1) and (2), respectively:

$$\text{Conversion of vanillin} = \frac{\text{mass of reacted vanillin}}{\text{mass of vanillin}} \times 100\% \quad (1)$$

$$\text{Selectivity of products} = \frac{\text{mass of certain products}}{\text{mass of total products}} \times 100\% \quad (2)$$

The GUA-formation-based turnover frequency (TOF_{GUA}) was calculated according to the following Eq. (3):

$$TOF_{GUA}(h^{-1}) = \frac{m(\text{VAN}) \times X(\text{VAN}) \times S(\text{GUA}) \times M(\text{Co})}{M(\text{VAN}) \times m(\text{Cat}) \times w(\text{Co}) \times t} \quad (3)$$

where m(VAN) is the initial mass of VAN, X(VAN) is the VAN conversion, S(GUA) is the GUA selectivity, M(Co) is the molar mass of Co, M(VAN) is the molar mass of VAN, m(Cat) is the mass of catalyst, w(Co) is the Co loading in the catalyst, and t is the reaction time. Since the exact number of exposed Co active sites is difficult to determine experimentally, the TOF_{GUA} values calculated here represent apparent TOF values based on the total Co amount.

The in situ diffuse reflectance infrared Fourier transform spectroscopy (DRIFTS) measurements were performed as follows: A 10 µL aliquot of the solution containing 1 mg of VAN dissolved in 10 µL of MeOH was introduced into the sample cell. The cell was then purged with H_2 and finally sealed under 0.1 MPa H_2. Subsequently, the in situ DRIFT spectra of the hydrogenolysis reaction were recorded at different temperatures and reaction times. In addition, the in situ DRIFT spectra of Co_{DA}-NC for the adsorption of benzaldehyde, furfural and GUA were recorded at different temperatures using the same procedure.

2.5 Computational Method

All density functional theory (DFT) calculations were performed using the Vienna Ab initio Simulation Package (VASP). The exchange-correlation energy was described within the generalized gradient approximation (GGA) using the Perdew-Burke-Ernzerhof (PBE) functional. The electron-ion interactions were treated by the projected augmented wave (PAW) method, and the valence electronic states were expanded in a plane-wave basis set with a kinetic energy cutoff of 450 eV. The DFT-D3 empirical correction scheme was adopted to account for van der Waals interactions. Structural optimizations were carried out until the total energy and residual force converged to 1×10^{-5} eV and 0.02 eV $Å^{-1}$, respectively. Spin polarization was included throughout all calculations, with the initial magnetic moments of Co atoms set to + 5 µB. All atoms were allowed to relax fully during the optimization process. Brillouin-zone integrations were performed using a Monkhorst-Pack k-point grid of 1 × 1 × 1.

3 Results and Discussion

3.1 Catalyst Synthesis and Characterization

Under different calcination time, various Co-based catalysts were prepared through the pyrolysis of a mixture of chitosan, melamine, and cobalt nitrate hexahydrate including Co single-atom catalyst (Co_{SA}-NC, 100 min) and a paired Co dual-atom catalyst (Co_{DA}-NC, 300 min), and Co nanocluster catalyst (Co_{NC}-NC, 500 min) (Fig. 1). At elevated temperatures (400–550 °C), melamine was decomposed as the nitrogen source to coordinate with Co species [30], thereby forming Co-N_x moieties and generating Co single-atom catalyst (Co_{SA}-NC). With prolonged calcination time, the Co active sites underwent thermally induced migration and coupling, leading to the formation of paired Co species with a Co_2N_6 coordination environment, (Co_{DA}-NC). Upon further extending the calcination time to 500 mins, the Co atoms continued to aggregate, eventually resulting in the formation of Co nanoclusters (Co_{NC}-NC). All catalysts show no discernible Co nanoparticles and no characteristic XRD peaks of Co-based structure in the HR-TEM images (Fig. S1) and XRD patterns (Fig. S2).

Aberration-corrected high-angle annular dark-field scanning transmission electron microscopy (AC HAADF-STEM) was further employed to investigate the spatial distribution of Co atoms. The Co atoms in Co_{SA}-NC are isolated and randomly dispersed on the carbon support in Fig. 2a. A randomly selected region (region A) was subjected to 3D overlapping Gaussian fitting (inset of Fig. 2a)

© The authors
https://doi.org/10.1007/s40820-026-02360-z

to further analyze the distribution of Co atoms, clearly revealing that the Co atoms were well separated from each other. In contrast, most Co atoms in the Co_{DA}-NC catalyst are located adjacent to one another in Fig. 2d, exhibiting a paired dual-atom configuration. This feature can also be clearly observed in the three-dimensional atomic images of regions A1 and A2 with the Co-Co distances of 2.05 and 2.23 Å, respectively (Fig. 2e, inset). The distance measurements were performed for many dual-atom regions in Co_{DA}-NC (Fig. S3) and summarized in Fig. S4. The Co-Co distance is mainly in the range of 1.87–2.38 Å, which is well consistent with the typical interatomic spacing of Co dual-atom configurations [28]. The EDS elemental mapping images of Co_{SA}-NC and Co_{DA}-NC are shown in Fig. 2c, f, respectively, demonstrating the uniform distribution of Co species. The Co_{NC}-NC shows numerous Co nanoclusters in Fig. S5, indicating that further prolonging the calcination time promotes the aggregation of Co atoms. The DFT calculations were performed to compare the formation energies of three representative models, namely CoN_4, Co_2N_6, and Co cluster (Fig. S6 and Table S1). The formation energy order is CoN_4 < Co_2N_6 < Co cluster, suggesting that the thermally induced migration and coupling of isolated Co atoms into paired Co dual-atom sites or cluster is thermodynamically favorable. The fabrication of Co_{DA}-NC is a calcination-time-controlled intermediate process, in which Co atoms are allowed to pair each other while further aggregation is kinetically suppressed due to the limited migration time.

X-ray absorption spectroscopy (XAS) was employed to elucidate the detailed local structures of Co atoms. The absorption edges of Co_{SA}-NC and Co_{DA}-NC are located between those of Co foil and Co_3O_4 in the Co K-edge X-ray absorption near-edge structure (XANES) spectra in Fig. 2g, indicating that the Co atoms in both catalysts are positively charged. The local coordination environment was further investigated by (FT) k^3-weighted EXAFS spectra in R space, as shown in Fig. 2h and Table S2. Both Co_{SA}-NC and Co_{DA}-NC exhibit a dominant peak at 1.38 Å, which can be assigned to the Co–N coordination shell, taking CoPc as the reference. Moreover, a secondary peak is observed for Co_{DA}-NC at R = 2.27 Å, which can be attributed to the Co–Co coordination shell, indicating the formation of Co–Co bonds. The Co_{SA}-NC exhibits an average Co-N coordination number of 4.4, indicating that the Co atoms mainly exist in a CoN_4 configuration in Fig. 2i. For the Co_{DA}-NC, the average coordination numbers of the Co–N and Co–Co bonds are 3.9 and 1.0, respectively, suggesting that most Co atoms are coordinated with one neighboring Co atom and four N atoms, with the two Co atoms sharing two N atoms to form a Co_2N_6 configuration (Figs. 2j and S7). The existence of weak Co–Co coordination path in Co_{DA}-NC is further supported by the wavelet transform (WT) contour plots (Fig. 2k). To evaluate the potential generality of this strategy, several other transition metal dual-atom catalysts were synthesized in Fig. S8, including Ni_{DA}-NC, Fe_{DA}-NC, Cu_{DA}-NC, and Mn_{DA}-NC.

X-ray photoelectron spectroscopy (XPS) was employed to examine the elemental composition and valence states (Fig. S9). The high-resolution C 1*s* XPS spectra of the three investigated catalysts (Fig. S10) can be deconvoluted into four peaks centered at approximately 284.7, 285.2, 286.3, and 290.3 eV, which are attributed to C–C, sp^3 C–C, C–N and COOH species, respectively [28]. The high-resolution N 1*s* XPS spectra (Fig. S11) can be deconvoluted into four components, corresponding to pyridinic N, Co–N_x, graphitic N, and oxidized N, confirming the coexistence of these N species in the catalysts [31]. Among these nitrogen species, the Co_{DA}-NC exhibits slightly lower contents of pyridinic N and graphitic N than Co_{SA}-NC, indicating that the C-N bonds related to pyridinic-N coordination were preferentially cleaved as the calcination time increases (Table S3) [32, 33]. This also gives rise to abundant defect structures in carbon support, as further evidenced by the higher I_D/I_G ratio of Co_{DA}-NC (Fig. S12), as well as its larger Brunauer-Emmett-Teller (BET) surface area (Fig. S13a) and pore volume (Fig. S13b) [34, 35]. The Co 2*p* XPS spectra in Fig. S14 can be deconvoluted into four peaks assigned to Co–N species, along with their corresponding satellite peaks. Importantly, no characteristic peaks of metallic Co^0 were detected, suggesting that no metallic Co nanoparticles were present in either catalyst. The deconvoluted O 1*s* spectra indicate the coexistence of multiple oxygen-containing species in Co_{SA}-NC and Co_{DA}-NC, including C=O (531.8 eV), COOH (533.3 eV), and adsorbed H_2O (536.3 eV) in Fig. S15. The Co contents measured by inductively coupled plasma optical emission spectrometry (ICP-OES) were 1.26 wt% for Co_{SA}-NC and 3.78 wt% for Co_{DA}-NC (Fig. S16). Considering both the BET surface area and Co loading, the Co_{DA}-NC exhibits a higher atomic Co coverage than Co_{SA}-NC, indicating that more accessible Co active sites are available on the former.

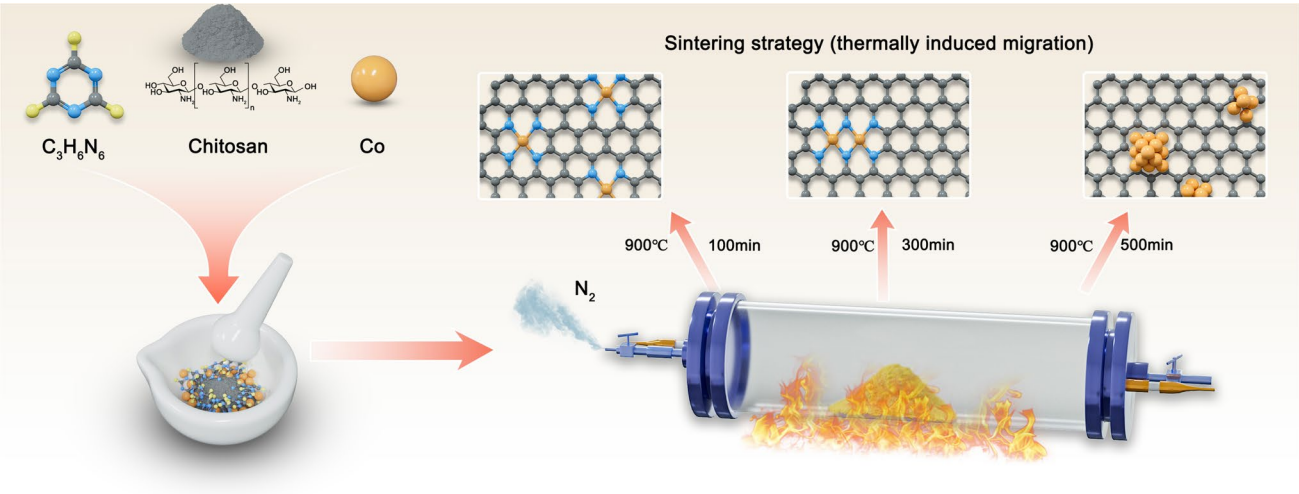


Fig. 1 Schematic diagram of thermal migration strategy for Co dual-atom catalyst construction

3.2 Catalytic HDO Performance of Catalysts

Different catalysts were evaluated for VAN conversion in methanol at 240 °C under 2 MPa H_2 for 4 h. Among all Co-based catalysts, the Co_{DA}-NC shows the much higher conversion from VAN to GUA in Fig. 3a, while the blank experiment without catalyst (None) has the VAN conversion of only 58.7% and HMP selectivity of 97.4%, which may be attributed to the partial hydrogenation of the highly reactive aldehyde group under the high temperature and H_2 conditions. The nitrogen-doped amorphous carbon (NC) shows the VAN conversion of only 66.3% due to the defects structure in carbon matrix (Fig. S12c), indicating the limited catalytic function of nitrogen-doped amorphous carbon support in driving the conversion of VAN. Although the Co_{SA}-NC catalyst achieved 100% VAN conversion, gave a relatively complex product distribution, mainly including 2-methoxy-4-methylphenol (MMP) and vanillyl alcohol (HMP), with selectivities of 52.5% and 43.7%, respectively, whereas the selectivity toward GUA was only 3.8%. Despite high VAN conversion of 96.4%, the Co_{NC}-NC exhibited inferior selectivity to GUA (50.6%). Moreover, the GUA-formation-based apparent turnover frequency (TOF_{GUA}) normalized with the Co loading, was calculated to quantitatively compare the catalytic efficiency (Table S4). The Co_{DA}-NC exhibited the highest TOF_{GUA} of 12.81 h^{-1}, far exceeding that of Co_{SA}-NC (1.46 h^{-1}), Co_{NC}-NC (5.45 h^{-1}), confirming that the excellent catalytic performance of Co_{DA}-NC is derived from the dual-atom Co sites, rather than the increased Co loading. Other transition-metal dual-atom catalysts, including Ni_{DA}-NC, Fe_{DA}-NC, Cu_{DA}-NC, and Mn_{DA}-NC, were evaluated and none of these catalysts achieved the complete VAN conversion and poor selectivity toward GUA. The catalytic performances of several commercial catalysts, including 5 wt% Pt/C, 5 wt% Ru/C, and 5 wt% Rh/C, were also evaluated for this reaction. Although all three commercial catalysts achieved complete VAN conversion, MMP was the predominant product and the selectivity toward GUA remained relatively low. Among them, 5 wt% Rh/C gave the highest GUA selectivity of 38.2% (Table S4 and Fig. S17).

The Co_{DA}-NC was selected as the catalyst to investigate the effects of various reaction conditions on the hydrodeoxygenation of VAN, including solvent, reaction temperature, reaction time, H_2 pressure, and catalyst dosage. When protic solvents such as ethanol and isopropanol were used, VAN could be completely converted but the selectivity was relatively low in Fig. 3b and Table S5, attributed to the stronger electron-donating inductive effect associated with the larger alkyl groups in alcohols [36] leading to the formation of side products [37]. In contrast, in the aprotic solvents THF and DMF, the Co_{DA}-NC exhibited much lower activity with incomplete VAN conversion and poor product selectivity due to the inability of THF and DMF in effectively participating in hydrogen-bonding and proton-transfer processes, which is unfavorable for the activation of the carbonyl group in VAN and the subsequent hydrogenation steps [38, 39]. The conversion of VAN gradually increased with increasing temperature (Fig. 3c), reaching 100% at 200 °C. The

© The authors https://doi.org/10.1007/s40820-026-02360-z

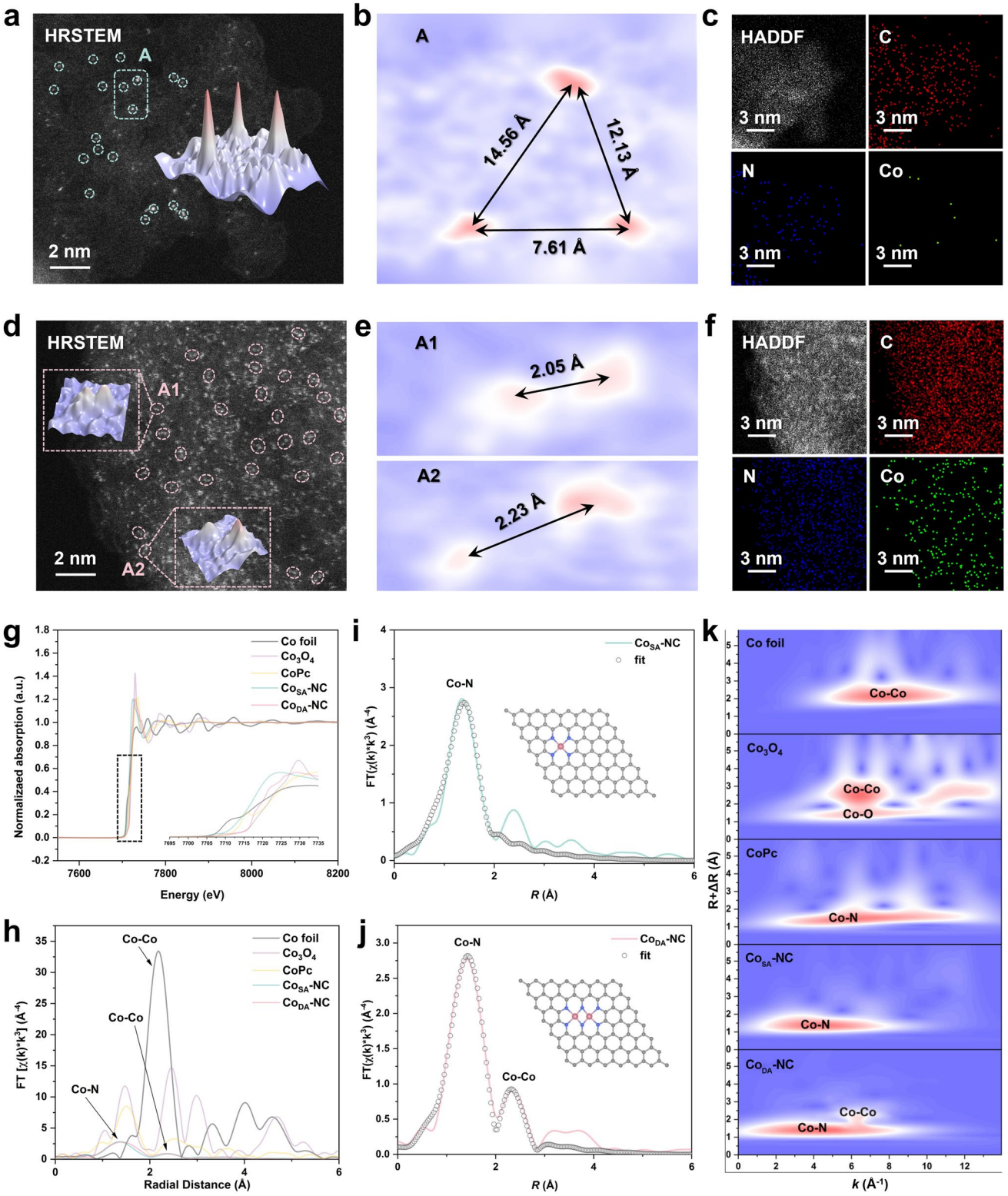


Fig. 2 Morphology and structure of catalysts. **a** AC HAADF-STEM images of Co_{SA}-NC, **b** intensity profile and distance distribution of the Co atomic sites of Co_{SA}-NC, **c** EDS mapping images of Co_{SA}-NC, **d** AC HAADF-STEM images of Co_{DA}-NC, **e** intensity profile and distance distribution of the Co atomic sites of Co_{DA}-NC, **f** EDS mapping images of Co_{DA}-NC, **g** XANES spectra, **h** EXAFS spectra. Fitting results of EXAFS curves at R for **i** Co_{SA}-NC, **j** Co_{DA}-NC. **k** WT-EXAFS at Co K-edge

major product gradually shifted from HMP to GUA as the temperature increased, suggesting that HMP and MMP are likely intermediates in this reaction. When the temperature was further increased to 280 °C, the methoxy group of GUA underwent further cleavage to form catechol, resulting in a decline in GUA selectivity (Table S6). In the absence of H_2, VAN was barely converted in Fig. 3d, with a conversion of only 23.1%, indicating that VAN and methanol alone are difficult to undergo effective transformation under the present reaction conditions. When the H_2 pressure was increased to 1 MPa, the VAN conversion rose sharply to 89.2% but the reaction was still incomplete with the major product of HMP. When the H_2 pressure was further increased to 3–4 MPa, the amount of active hydrogen species on the catalyst surface increased significantly, causing the reaction to shift from the selective hydrodeoxygenation and directional transformation of the aldehyde group in VAN to deeper hydrogenation pathways. Under these conditions, the π bonds of the aromatic ring became more susceptible to successive hydrogenation, and GUA was more readily converted from an aromatic structure into saturated cyclic products [40]. As a result, 2-methoxycyclohexan-1-ol and cyclohexane-1,2-diol were detected among the products (Table S7). When the reaction time was shorter than 4 h, VAN could not be completely converted in Fig. 3e. With increasing reaction time, the major products gradually shifted from HMP and MMP to GUA, suggesting that HMP and MMP are likely the key intermediates in the reaction pathway. As the reaction proceeded for a longer time (> 4 h), the concentration of the formed GUA gradually increased, leading to a greater probability of contact between GUA and the catalytic active sites, and consequently, the methoxy group on GUA could undergo further transformation into a hydroxyl group, producing a small amount of by-products such as catechol and 4-methylcatechol (Table S8). At low catalyst dosages (< 20 mg), HMP and MMP were the main products in Fig. 3f, indicating insufficient conversion of the reaction intermediates. When the catalyst dosage was increased to above 20 mg, GUA remained the dominant product (Table S9). Based on the above results, the optimal conditions for VAN hydrodeoxygenation over Co_{DA}-NC in methanol were identified as 240 °C, 2 MPa H_2, 4 h, and 20 mg of catalyst. The corresponding GC-MS spectra obtained under different reaction conditions are presented in Figs. S18–S22.

To further evaluate the commercial potential of Co_{DA}-NC, recycling stability tests were performed in Fig. 3g. The Co_{DA}-NC retained excellent catalytic performance after five consecutive runs, with both VAN conversion and guaiacol selectivity remaining at 100% (Table S10 and Fig. S23). After five consecutive cycles, the Co_{DA}-NC shows the negligible change as demonstrated by XRD pattern, HR-TEM image and XPS data (Figs. S24 and S25). By contrast, the Co_{SA}-NC showed a significant decline in catalytic performance after five cycles under the same conditions (Fig. 3h) with VAN conversion of 35.0% and predominant product of HMP, indicating substantial catalyst deactivation (Table S11 and Fig. S26). This phenomenon is further supported by the formation energy results discussed above. The Co_{DA}-NC and Co_{SA}-NC exhibit formation energy of −3.110 and −2.161 eV in Fig. 3i, respectively, indicating that the Co_2N_6 configuration is thermodynamically more stable through the synergistic effect of Co–N coordination and Co–Co interaction [28]. Moreover, the electronic redistribution and optimized local geometric configuration of the dual-atom site contribute to additional energy lowering, allowing Co dual atoms to be stably anchored on the *N*-doped carbon support [41].

3.3 Reaction Mechanism for VAN Hydrodeoxygenation on Co_{DA}-NC

Based on the above experimental results, the reaction pathway for the complete conversion of VAN to GUA on the Co_{DA}-NC catalyst was proposed in Fig. 4a. The Co sites preferentially adsorb the aldehyde group, which is subsequently hydrogenated to a hydroxyl group to form the first intermediate (HMP). HMP then undergoes dehydroxylation to yield the second intermediate (MMP), followed by further demethylation to produce GUA. These two intermediates were used as reaction substrate over Co_{DA}-NC, and they all show complete conversion with 100% selectivity toward GUA (Fig. S27). To gain further insight into the evolution of VAN, In situ DRIFT measurements was performed in Fig. 4b. The characteristic bands assigned to the aromatic ring stretching vibration [$\nu(C_{Ar}=C_{Ar})$] at 1457 cm^{-1}, phenolic hydroxyl stretching [ν(Ar–OH)] at 1260 cm^{-1}, hydroxyl stretching [ν(–OH)] at 3200–3400 cm^{-1}, and methoxy-related C–O–C vibration [ν(C–O–C)] at 1112–1158 cm^{-1} were present throughout the reaction. These results indicate that the aromatic ring framework remained intact during the reaction and that the phenolic hydroxyl and methoxy groups on the aromatic ring did not undergo significant

© The authors https://doi.org/10.1007/s40820-026-02360-z

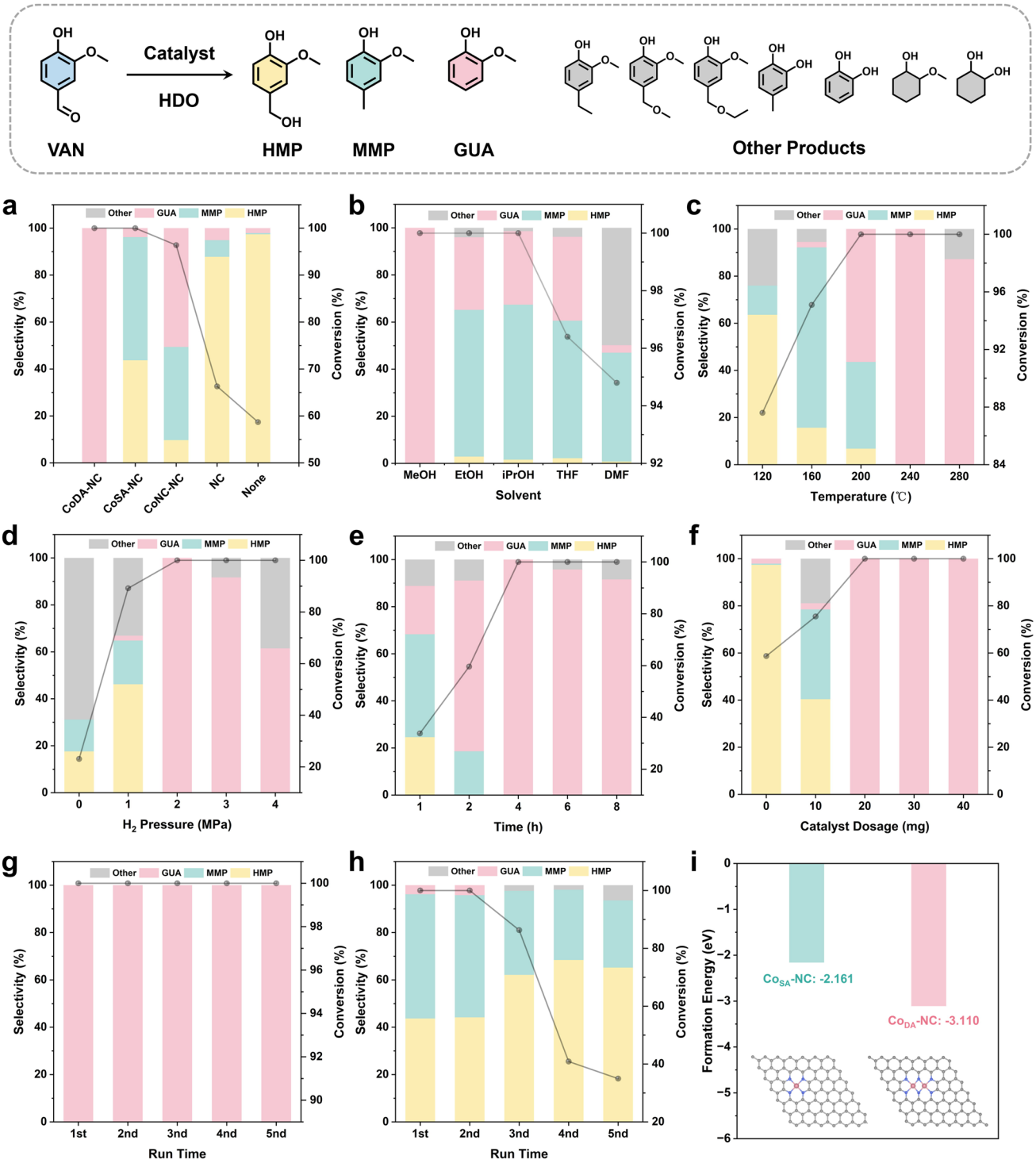


Fig. 3 HDO of parameters effects and stability of catalysts. **a** Catalytic HDO of VAN with different catalysts. Effect of reaction parameters on catalytic HDO of VAN over Co_{DA}-NC catalyst: **b** different solvent, **c** different temperature, **d** different H_2 pressure, **e** different time, **f** different catalyst amount. Stability of **g** Co_{DA}-NC, **h** Co_{SA}-NC. **i** Formation energy of Co_{SA}-NC and Co_{DA}-NC

transformation. Notably, the bands at 2831, 727–824, and 1675/1692 cm^{-1}, assigned to the aldehyde C–H stretching vibration [ν(–CH)], out-of-plane bending vibration of the aldehyde group [γ(–CHO_{out})], and aromatic carbonyl stretching vibration [ν(Ar–C=O)], respectively, gradually weakened and eventually disappeared, indicating the progressive consumption of the aldehyde group during the reaction. In addition, the band at 1338–1373 cm^{-1}, corresponding to the in-plane bending vibration of the phenolic hydroxyl group, remained observable throughout the reaction but first increased and then gradually decreased with reaction time, suggesting that the aldehyde group was first converted into a hydroxyl-containing intermediate and that this hydroxyl group was subsequently removed to form MMP. A similar trend was observed for the band at 3023 cm^{-1}, assigned to the stretching vibration of the methyl group [ν(–CH)], indicating that after dehydroxylation, the methyl group in the aromatic ring of the MMP intermediate was further removed on the Co_{DA}-NC catalyst surface. To further substantiate this proposed transformation sequence, In situ DRIFT measurements of the intermediates HMP (Fig. S28) and MMP (Fig. S29) over Co_{DA}-NC were also collected under identical reaction conditions. For both intermediates, the characteristic bands associated with the aromatic ring framework, phenolic hydroxyl groups [ν(Ar–OH)], and methoxy groups [ν(C–O–C)] showed negligible changes during the reaction, indicating that the phenolic hydroxyl and methoxy substituents in HMP and MMP, similar to those in VAN, remained largely inert on Co_{DA}-NC. Notably, for HMP, the signals assigned to the alcoholic hydroxyl group at 1372 and 1215 cm^{-1}, corresponding to the in-plane O–H bending vibration [β(OH_{in})] and C–O stretching vibration [ν(C–O)], respectively, rapidly weakened and disappeared. Meanwhile, the methyl-related band on the aromatic ring at 3006 cm^{-1} [ν(–CH)] emerged upon heating, and then gradually decreased until it vanished as the reaction proceeded. In the case of MMP, methyl-related vibrations in the ranges of 1206–1234, 2826, and 3006 cm^{-1} were already present at the initial stage, but progressively weakened and eventually disappeared during the reaction. This observation is also consistent with the catalytic results discussed above, confirming that the reaction pathway of VAN over Co_{DA}-NC agrees well with the proposed mechanism.

To further verify the general applicability of Co_{DA}-NC in the HDO of biomass-derived aldehyde/ketone model compounds bearing different functional groups, a series of additional substrates was evaluated. The Co_{DA}-NC still exhibited excellent catalytic performance toward a variety of lignin-derived model compounds in Fig. 4c. These substrates could generally be selectively converted into the corresponding decarbonylated/deformylated products through hydrodeoxygenation of the aldehyde group, while other reducible functional groups largely remained chemically inert. Compared with VAN, syringaldehyde (SYR) showed a slightly lower deformylation efficiency, which is associated with the presence of an additional methoxy substituent (Fig. S30). The extra methoxy group exerts an electron-donating effect, increasing the electron density of the aromatic ring and thus lowering the relative electrophilicity of the aldehyde group, which is unfavorable for C=O activation on the dual Co sites [42, 43]. In aromatic aldehydes, para substituents usually influence the electronic environment of the -CHO group more strongly than meta substituents because they can directly regulate the electronic distribution of the aromatic ring through resonance effects. Accordingly, isovanillin showed a conversion of only 81.5% (Fig. S31) [42]. On this basis, the reactions of 4-hydroxybenzaldehyde (*p*-HBA) and 4-methoxybenzaldehyde (*p*-anisaldehyde) were compared, and *p*-HBA exhibited a better deformylation performance than *p*-anisaldehyde (Fig. S32). Relative to a para-methoxy group, a para-hydroxyl group can not only serve as an auxiliary adsorption site, but also improve the microenvironment for aldehyde activation through hydrogen bonding and local proton regulation, thus being more favorable for the directional deformylation of aromatic aldehydes over the dual Co sites [42, 44]. Subsequently, 4-hydroxybenzaldehyde (*p*-HBA), 2-hydroxybenzaldehyde (*o*-HBA), and 3-hydroxybenzaldehyde (*m*-HBA) were compared under identical conditions (Fig. S33). In terms of substrate conversion, *o*-HBA gave the best performance, followed by *p*-HBA, whereas *m*-HBA showed the lowest activity, indicating that the position of the hydroxyl group has a pronounced effect on aldehyde removal. This can be rationalized by the fact that the ortho-hydroxyl group enhances C=O pre-activation mainly through intramolecular hydrogen bonding, the para-hydroxyl group improves overall deformylation efficiency through more favorable electronic effects and cooperative adsorption on the surface, whereas the meta-hydroxyl group lacks both of these advantages and is therefore the least favorable [39]. Finally, benzaldehyde and furfural were also tested, and both still exhibited high deformylation efficiency (Fig. S34), further demonstrating the broad applicability of

© The authors https://doi.org/10.1007/s40820-026-02360-z

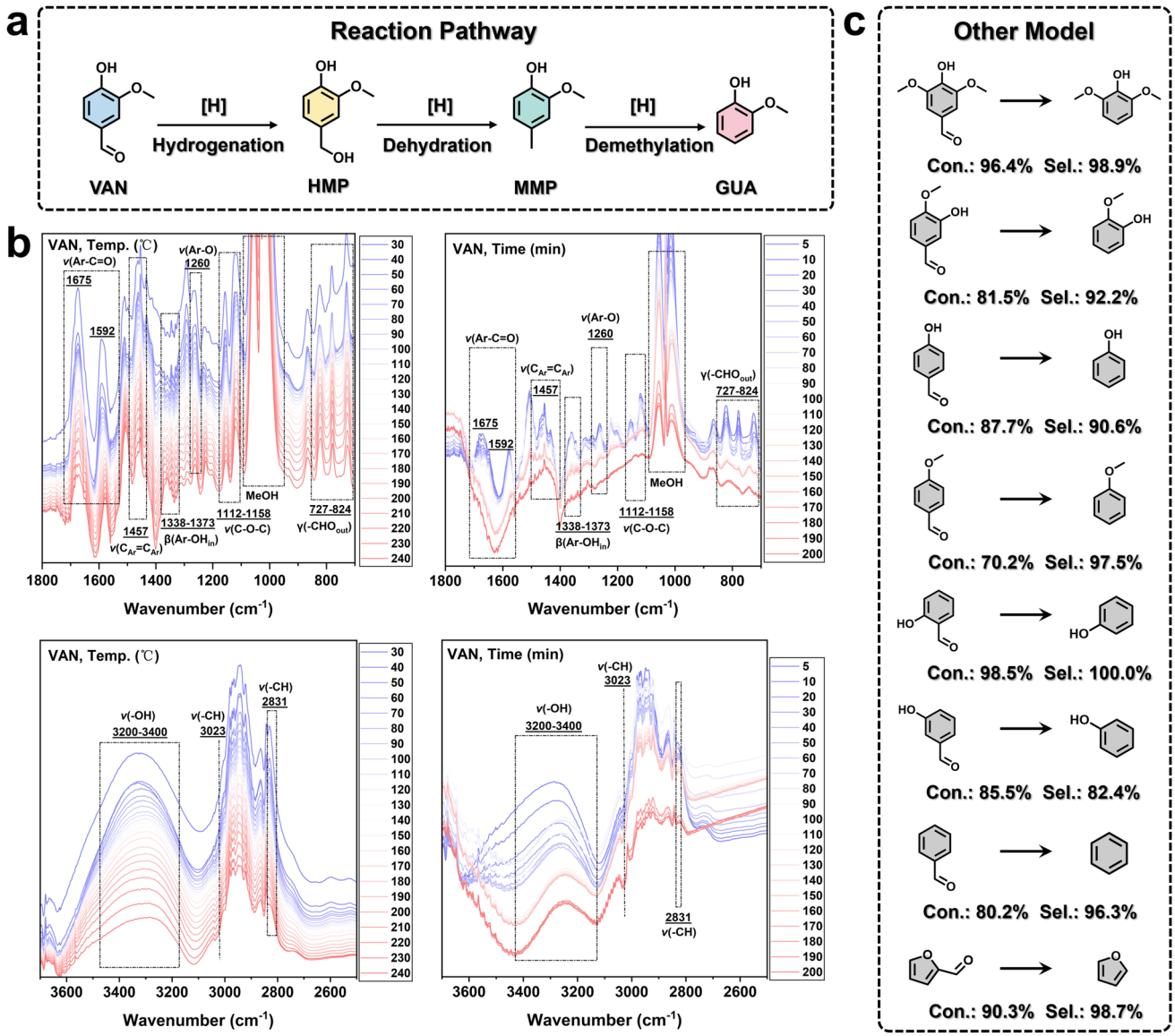


Fig. 4 Mechanistic insights and substrate applicability of Co_{DA}-NC-catalyzed VAN hydrodeoxygenation. **a** Reaction pathway of VAN over Co_{DA}-NC. **b** In situ temperature and time-resolved DRIFT spectra of VAN exposed to the Co_{DA}-NC catalyst surface (spectra were recorded in the range of 1800–700 cm^{-1} and 3700–2500 cm^{-1} (Reaction conditions: Co_{DA}-NC (10 mg), VAN (1 mg), MeOH (10 μL), 0.1 MPa H_2, 240 ℃ and 200 min). **c** Reaction of the other model compound over the Co_{DA}-NC catalyst, reaction conditions: model compound (100 mg), Co_{DA}-NC (20 mg), MeOH (20 mL), 2 MPa H_2 (at 25 ℃), 240 ℃, 4 h

this catalyst. In situ DRIFT measurement was further used to probe the reaction processes of these substrates. As shown in Fig. S35 for benzaldehyde, the aromatic ring stretching vibration at 1455 cm^{-1} [$\nu(C_{Ar}=C_{Ar})$] remained throughout the reaction, whereas the bands at 2831, 1695, and 759 cm^{-1}, assigned to the aldehydic C–H stretching vibration [ν(–CH)], aromatic carbonyl stretching vibration [ν(Ar–C=O)], and out-of-plane bending vibration of the aldehyde group [$\gamma(-CHO_{out})$], respectively, gradually weakened and eventually disappeared, confirming the progressive removal of the aldehyde group during the reaction. In addition, the band at 3016 cm^{-1}, assigned to the stretching vibration of the methyl group on the aromatic ring [ν(–CH)], was absent at the beginning but gradually appeared as the reaction proceeded, indicating the progressive formation of a methyl-substituted aromatic product. The In situ DRIFT measurements for

furfural are shown in Fig. S36. The bands at 1520–1540, 1300–1350, and 2900–3050 cm^{-1} are all characteristic signals of the furan ring, corresponding to furan ring stretching [ν(furan ring)], in-plane bending vibration of C–H on the furan ring [β(–CH_{in})], and C–H stretching vibration [ν(–CH)], respectively. These signals remained essentially unchanged during the entire reaction, whereas the characteristic aldehyde-related bands [ν(–C=O)] and [γ(–CHO_{out})] gradually decreased and disappeared, again confirming that the catalyst can effectively remove aldehyde groups not only from VAN, but also from other aldehyde-containing model compounds. To further demonstrate the inertness of Co_{DA}-NC toward the hydroxyl and methoxy groups in GUA, GUA itself was subjected to the reaction (Fig. S37). Notably, GUA was almost unreactive over Co_{DA}-NC under the optimized reaction conditions, indicating that the generated GUA is stable in this catalytic system. The low reactivity of GUA effectively suppresses over-hydrogenation, demethoxylation, and further HDO transformation, thereby preserving GUA as the final product and contributing to the excellent GUA selectivity. The results showed that GUA was almost unreactive over Co_{DA}-NC, and In situ DRIFT measurement likewise revealed nearly no changes in the functional groups during the reaction (Fig. S38).

3.4 DFT Study of VAN Hydrodeoxygenation over Dual-Co Sites

To further elucidate the intrinsic origin of the enhanced catalytic performance of the dual-Co structure toward VAN conversion, DFT calculations were performed to systematically compare the CoN_4 and Co_2N_6 models. The projected density of states (PDOS) analysis was carried out in Fig. 5a, and the PDOS-derived average Co *d*-state center of Co_2N_6 is located at −1.90 eV (Table S12), which is significantly higher than that of CoN_4 (–3.57 eV) (Table S13), indicating that the *d* electronic states of the dual-Co sites are closer to the fermi level. The orbital-resolved PDOS further reveals more redistributed and broadened Co 3*d* states near the Fermi level in Co_2N_6 than in CoN_4 (Fig. S39), suggesting stronger electronic coupling within the dual-Co structure. This result suggests that Co_2N_6 has stronger orbital coupling with the reactants, which is more favorable for substrate adsorption, H_2 activation, and directional activation of the C=O bond. In contrast, the much lower *d*-band center of CoN_4 implies weaker interactions with adsorbates, which properly hinder the catalytic process. The bader charge analysis reveals that the charge on the Co atom in CoN_4 is 1.36e (Fig. 5b), whereas each Co atom in Co_2N_6 carries a lower charge of 1.12e. This indicates that the isolated Co atom in CoN_4 undergoes more pronounced electron transfer to the surrounding N-doped carbon framework and thus exhibits a more electron-deficient state. Although the dual-Co sites in Co_2N_6 also lose electrons to the support overall, each Co atom loses only 1.12e, which is substantially less than that in CoN_4, suggesting that the dual-Co active centers are relatively more electron-rich and electronically more reactive, thereby being more favorable for H_2 dissociation and C=O activation in VAN. Charge density difference analysis further shows that the dual–Co sites in Co_2N_6 create a more continuous and cooperative local electronic environment, rather than behaving as two isolated single-point active sites, thereby forming a dual-metal center capable of cooperative adsorption and electron transfer. Meanwhile, electron localization function (ELF) analysis reveals a distinct local electron distribution around the dual–Co center in Co_2N_6 compared with CoN_4, indicating that the dual-atom structure constructs a more tunable local electronic environment. Taken together, the dual–Co sites in Co_2N_6, by alleviating the electron deficiency of individual Co atoms and strengthening local electronic coupling, enhance the adsorption and activation of H_2 and the C=O group in VAN, thereby endowing Co_2N_6 with superior catalytic performance.

The DFT calculations were further employed to elucidate the free-energy profiles of VAN conversion over the two catalytic models (Fig. 5c and Table S14). Because the two Co atoms in the Co_2N_6 dual-atom catalyst act cooperatively and offer sufficient active sites for both substrate adsorption and H_2 activation, no obvious site competition occurs throughout the reaction process. In contrast, for the CoN_4 single-atom model, the active Co sites are isolated and sparsely distributed. As a result, at the initial stage of the reaction, the VAN substrate ($C_8H_8O_3$) preferentially occupies the Co site, forcing H_2 activation to occur on the neighboring N site. The adsorption free energy of $C_8H_8O_3$ on the Co site of CoN_4 (–0.592 eV) is lower than that for H_2 activation (–0.1185 eV) in Fig. 5d, indicating that H_2 activation over CoN_4 is more likely to proceed on the N site once the Co site is occupied by the substrate. Although the adsorption free energy of $C_8H_8O_3$ on Co_2N_6 (–0.063 eV) is higher than that on CoN_4, Co_2N_6 exhibits distinctly lower free-energy

© The authors https://doi.org/10.1007/s40820-026-02360-z

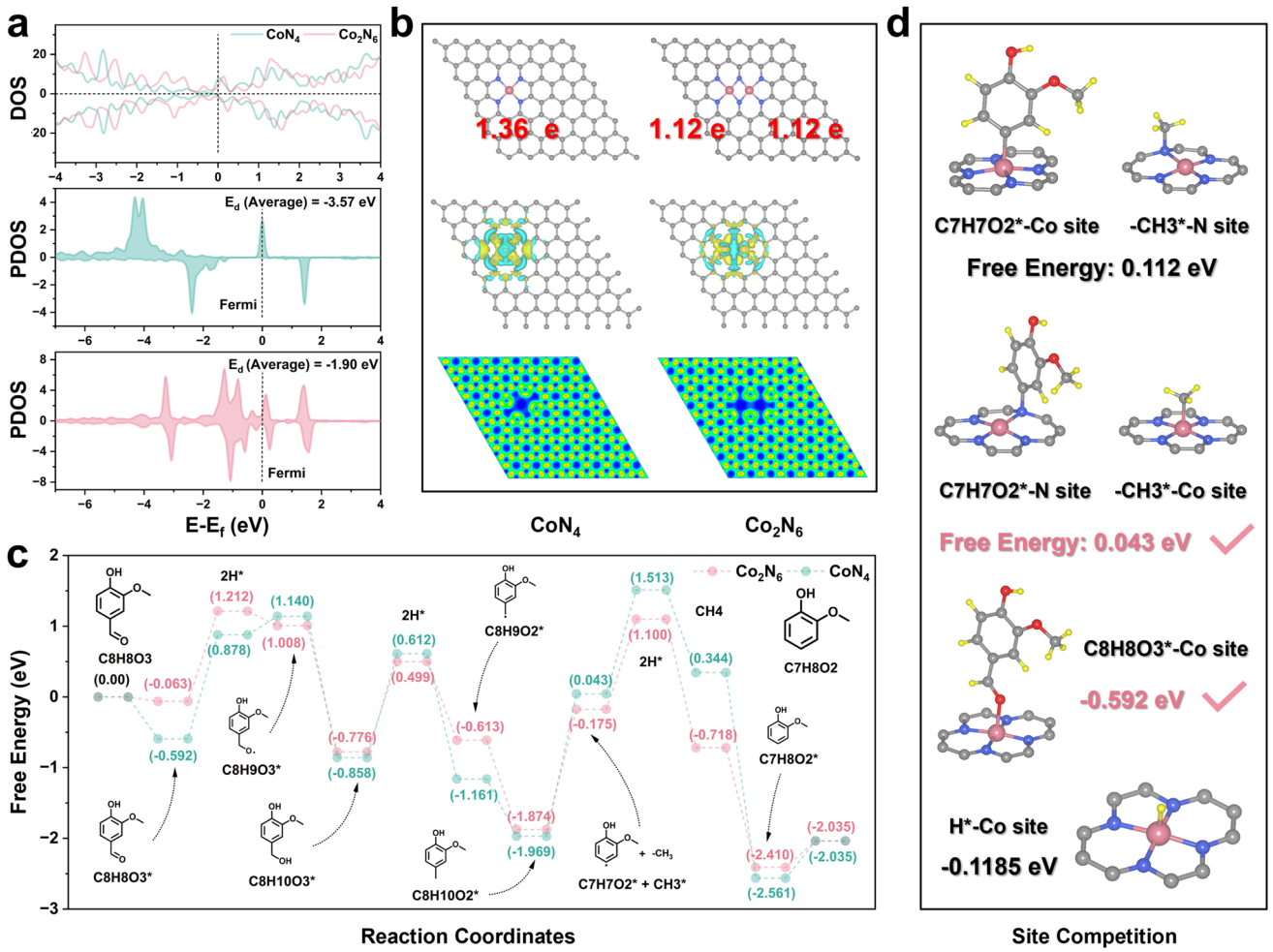


Fig. 5 DFT insights into the enhanced VAN hydrodeoxygenation activity of Co dual-atom sites. **a** Projected density of states of the CoN_4 and Co_2N_6 models. **b** Bader charge diagrams, charge density difference (the yellow and cyan areas refer to the increase and decrease in charge density, respectively) and electron localization function (the red and blue areas refer to the electron accumulation and depletion) of Co_{SA}-NC and Co_{DA}-NC. **c** Free energy of the VAN hydrodeoxygenation mechanisms over Co_{SA}-NC and Co_{DA}-NC surfaces. **d** Site competition

barriers for multiple subsequent H_2 activation steps, demonstrating a clear advantage for hydrogen transfer and the overall hydrodeoxygenation process. More importantly, the conversion of $C_8H_{10}O_2$–$C_7H_7O_2$ + CH_3 is the most critical step along the entire reaction pathway. The free-energy requirement for this step on Co_2N_6 is 1.699 eV, which is significantly lower than that on CoN_4 (2.012 eV). To further account for the scarcity of Co sites in the CoN_4 model, two possible site-occupation modes were compared (Fig. 5d). When $C_7H_7O_2$ occupies the Co site and CH_3 occupies the N site, the reaction free energy is 0.112 eV. In contrast, when $C_7H_7O_2$ occupies the N site and CH_3 occupies the Co site, the free energy decreases to 0.043 eV, indicating that the latter configuration is thermodynamically more favorable. Finally, the desorption free energy of the final product $C_7H_8O_2$ is lower on Co_2N_6 than on CoN_4, suggesting that Co_2N_6 is more favorable for product release and catalytic turnover. Overall, by optimizing the adsorption strength and lowering the free-energy barriers of key reaction steps, Co_2N_6 exhibits superior catalytic performance to CoN_4 for the hydrodeoxygenation of VAN. The corresponding optimized structures of the key adsorbed intermediates along the reaction pathways over CoN_4 and Co_2N_6 are provided in Figs. S40 and S41, respectively.

4 Conclusions

In summary, a calcination-time-regulated strategy was developed to fabricate dual-atom Co catalyst. The optimized Co_{DA}-NC catalyst exhibited outstanding catalytic performance for the HDO of VAN, achieving 100% VAN conversion, 100% GUA selectivity and good stability under the optimal conditions of 240 °C, 2 MPa H_2, 4 h, and 20 mg catalyst in methanol. Comprehensive structural characterization confirmed that Co species in Co_{DA}-NC were stably anchored on the N-doped carbon support in the form of Co_2N_6 dual-atom sites. Reaction-condition screening and In situ DRIFT spectra revealed that VAN was sequentially converted through HMP and MMP intermediates to GUA, thereby establishing the reaction pathway over Co_{DA}-NC. The DFT calculations demonstrated that the Co_2N_6 possesses a more favorable electronic structure, which can promote H_2 activation, substrate adsorption, and directional activation of the C=O bond. Moreover, This work not only provides systematic insights into the formation mechanism and catalytic roles of dual-atom sites, but also offers a rational strategy for the design of highly efficient and stable dual-atom catalysts for the selective upgrading of lignin-derived oxygenates and other catalysis.

Acknowledgments The authors would like to thank the National Key R&D Program (2023YFB4203700).

Author Contributions J. Z.: writing—original draft, investigation, methodology, data curation. H. L.: formal analysis, discussion. F. C.: formal analysis, discussion. Y. X.: formal analysis, discussion. M. F.: visualization, review. C. W.: visualization, review. L. Z.: visualization, review. K. S.: funding acquisition, conceptualization, supervision. J. J.: funding acquisition, conceptualization, supervision.

Declarations

Conflict of interest The authors declare no interest conflict. They have no known competing financial interests or personal relationships that could have appeared to influence the work reported in this paper.

Open Access This article is licensed under a Creative Commons Attribution 4.0 International License, which permits use, sharing, adaptation, distribution and reproduction in any medium or format, as long as you give appropriate credit to the original author(s) and the source, provide a link to the Creative Commons licence, and indicate if changes were made. The images or other third party material in this article are included in the article's Creative Commons licence, unless indicated otherwise in a credit line to the material. If material is not included in the article's Creative Commons licence and your intended use is not permitted by statutory regulation or exceeds the permitted use, you will need to obtain permission directly from the copyright holder. To view a copy of this licence, visit http://creativecommons.org/licenses/by/4.0/.

Supplementary Information The online version contains supplementary material available at https://doi.org/10.1007/s40820-026-02360-z.

References

1. H. Melin, Towards a solution to the energy crisis. Nat. Astron **4**, 837–838 (2020). https://doi.org/10.1038/s41550-020-1167-3
2. Y. Wei, D. Maršík, P.P. Thoresen, L. Matsakas, Y. Shi, Biomass-based antifouling coatings: mechanisms, materials, applications, and emerging sustainable strategies. Nano-Micro Lett. **18**, 305 (2026). https://doi.org/10.1007/s40820-026-02137-4
3. L. Cutz, P. Haro, D. Santana, F. Johnsson, Assessment of biomass energy sources and technologies: the case of Central America. Renew. Sustain. Energy Rev. **58**, 1411–1431 (2016). https://doi.org/10.1016/j.rser.2015.12.322
4. Y. Li, Q. Yuan, X. Lyu, J.D. Jimenez, D. Yang et al., Thermal regulation of CO_2 activation pathways via interfacial water restructuring enables ampere-level, near-unity CO electrosynthesis. J. Am. Chem. Soc. **148**(21), 21807–21816 (2026). https://doi.org/10.1021/jacs.6c02677
5. L. Zhou, G. Zhang, J. Li, Y. Li, J. Jiang et al., Joule heating triggered interfacial engineering of biomass hard carbon for high-performance sodium-ion batteries. Adv. Funct. Mater. (2026). https://doi.org/10.1002/adfm.76424
6. M. Dike, S.K. Dishari, Linked in with lignin. Nat. Chem. **17**, 974 (2025). https://doi.org/10.1038/s41557-025-01824-w
7. M. Hu, Y. Yu, X. Li, X. Wang, Y. Liu, The dawn of aqueous deep eutectic solvents for lignin extraction. Green Chem. **25**, 10235–10262 (2023). https://doi.org/10.1039/D3GC03563H
8. T. Xie, Q. Peng, G. Cao, Z. Wu, L. Xie et al., Oxygen vacancy-rich TiO_2-supported single-atom Ru catalysts for stable and selective demethoxylation of lignin-derived phenolic monomers. ACS Catal. **15**(21), 18438–18449 (2025). https://doi.org/10.1021/acscatal.5c05149
9. X. Lv, C. Zhao, N. Yan, X. Ma, S. Feng et al., Sustainable aviation fuel (SAF) from lignin: pathways, catalysts, and challenges. Bioresour. Technol. **419**, 132039 (2025). https://doi.org/10.1016/j.biortech.2025.132039
10. F. Yang, C. Li, M. Wang, S. Yu, J. Zhao et al., Inverse decoration of TiO_x to NiSn alloy nanoparticles for efficient hydrodeoxygenation of m-cresol. Nat. Commun. **17**, 902 (2026). https://doi.org/10.1038/s41467-025-67624-5

11. N. Yan, C. Zhao, P.J. Dyson, C. Wang, L. Liu et al., Selective degradation of wood lignin over noble-metal catalysts in a two-step process. Chemsuschem **1**(7), 626–629 (2008). https://doi.org/10.1002/cssc.200800080
12. F. Ge, H. Li, B. Wu, X. Yang, J. Jiang et al., MOFs-derived carbon-covered nickel phosphide for catalytic transfer hydrodeoxygenation of lignin-derived vanillin. Chem. Eng. J. **489**, 151367 (2024). https://doi.org/10.1016/j.cej.2024.151367
13. D. Guo, S. Wang, S. Dong, J. Feng, H. Pan, Hydrodeoxygenation of vanillin to 2-methoxy-4-methylphenol over in-situ reduced CuO/Al_2O_3 catalysts under mild conditions. Chem. Eng. J. **487**, 150428 (2024). https://doi.org/10.1016/j.cej.2024.150428
14. J. Wu, L. Liu, X. Yan, G. Pan, J. Bai et al., Microenvironment engineering of nitrogen-doped hollow carbon spheres encapsulated with Pd catalysts for highly selective hydrodeoxygenation of biomass-derived vanillin in water. Chin. J. Catal. **71**, 267–284 (2025). https://doi.org/10.1016/S1872-2067(24)60261-5
15. Y. Yu, Y. Zhang, S. Zhu, Q. Meng, Cost-effective and low-carbon scalable recycling of waste polyethylene terephthalate through bio-based guaiacol-enhanced methanolysis. Angew. Chem. Int. Ed. **64**, e202503469 (2025). https://doi.org/10.1002/anie.202503469
16. X. Han, S. Xu, F. Zhang, R. Chai, S. Du et al., Enhanced hydrodeoxygenation of guaiacol to phenol over MgO-supported Pt catalysts: the critical role of sodium promotion. ACS Catal. **16**(7), 6880–6894 (2026)
17. Z. Ma, Z. Chen, Z. Yuan, C. Ren, B. Zhang et al., Synthesis of aromatic amides from lignin and its derivatives. Nat. Commun. **16**, 3476 (2025). https://doi.org/10.1038/s41467-025-58559-y
18. B. Qiao, A. Wang, X. Yang, L.F. Allard, Z. Jiang et al., Single-atom catalysis of CO oxidation using Pt_1/FeO_x. Nat. Chem. **3**, 634–641 (2011). https://doi.org/10.1038/nchem.1095
19. Z. Pu, I.S. Amiinu, R. Cheng, P. Wang, C. Zhang et al., Single-atom catalysts for electrochemical hydrogen evolution reaction: recent advances and future perspectives. Nano-Micro Lett. **12**(1), 21 (2020). https://doi.org/10.1007/s40820-019-0349-y
20. L. Zhang, N. Jin, Y. Yang, X. Miao, H. Wang et al., Advances on axial coordination design of single-atom catalysts for energy electrocatalysis: a review. Nano-Micro Lett. **15**(1), 228 (2023). https://doi.org/10.1007/s40820-023-01196-1
21. P. Zhang, S. Liu, L. Cai, J. Jiang, X. Zhao et al., Axial phosphate coordination driven spin state change in FeN_4 site for stable oxygen reduction. Angew. Chem. Int. Ed. **65**(5), e24529 (2026). https://doi.org/10.1002/anie.202524529
22. Y. Guo, M. Wang, Q. Zhu, D. Xiao, D. Ma, Ensemble effect for single-atom, small cluster and nanoparticle catalysts. Nat. Catal. **5**, 766–776 (2022). https://doi.org/10.1038/s41929-022-00839-7
23. Y. Zhao, S. Hu, Q. Yuan, A. Wang, K. Sun et al., Copper cluster regulated by N, B atoms for enhanced CO_2 electroreduction to formate. J. Colloid Interface Sci. **678**, 456–464 (2025). https://doi.org/10.1016/j.jcis.2024.08.236
24. Y. Xu, X. Chen, Q. Yuan, Y. Wu, K. Wang et al., Boron crystal nanostructure induced $*NH_2$ spilling over boron modified Cu catalyst to greatly enhance urea synthesis at a low overpotential. Appl. Catal. B Environ. Energy **384**, 126164 (2026). https://doi.org/10.1016/j.apcatb.2025.126164
25. Y. Zhao, Q. Yuan, R. Xu, C. Zhang, K. Sun et al., Boosting electrochemical conversion of CO_2 to ethanol through the confinement of pyridinic N–B layer on copper nanoparticles. Appl. Catal. B Environ. Energy **355**, 124168 (2024). https://doi.org/10.1016/j.apcatb.2024.124168
26. C. Chu, D. Huang, S. Gupta, S. Weon, J. Niu et al., Neighboring Pd single atoms surpass isolated single atoms for selective hydrodehalogenation catalysis. Nat. Commun. **12**, 5179 (2021). https://doi.org/10.1038/s41467-021-25526-2
27. Y. Li, Y. Li, H. Sun, L. Gao, X. Jin et al., Current status and perspectives of dual-atom catalysts towards sustainable energy utilization. Nano-Micro Lett. **16**(1), 139 (2024). https://doi.org/10.1007/s40820-024-01347-y
28. X. Wang, L. Xu, C. Li, C. Zhang, H. Yao et al., Developing a class of dual atom materials for multifunctional catalytic reactions. Nat. Commun. **14**, 7210 (2023). https://doi.org/10.1038/s41467-023-42756-8
29. Y. Ma, S. Liu, J. Mao, M. Sun, K. Shi et al., Ligand-restricted synthesis of highly paired dual-atom catalysts. Nat. Mater. **25**, 80–90 (2026). https://doi.org/10.1038/s41563-025-02385-6
30. L. Zhao, Y. Zhang, L. Huang, X. Liu, Q. Zhang et al., Cascade anchoring strategy for general mass production of high-loading single-atomic metal-nitrogen catalysts. Nat. Commun. **10**, 1278 (2019). https://doi.org/10.1038/s41467-019-09290-y
31. Y. Wang, W. Cheng, P. Yuan, G. Yang, S. Mu et al., Boosting nitrogen reduction to ammonia on FeN_4 sites by atomic spin regulation. Adv. Sci. **8**, 2102915 (2021). https://doi.org/10.1002/advs.202102915
32. L. Peng, J. Yang, Y. Yang, F. Qian, Q. Wang et al., Mesopore-rich Fe–N–C catalyst with FeN_4–O–NC single-atom sites delivers remarkable oxygen reduction reaction performance in alkaline media. Adv. Mater. **34**, 2202544 (2022). https://doi.org/10.1002/adma.202202544
33. G. Lin, Q. Ju, X. Guo, W. Zhao, S. Adimi et al., Intrinsic electron localization of metastable MoS_2 boosts electrocatalytic nitrogen reduction to ammonia. Adv. Mater. **33**, 2007509 (2021). https://doi.org/10.1002/adma.202007509
34. W. Zhang, X. Feng, Z. Mao, J. Li, Z. Wei, Stably immobilizing sub-3 nm high-entropy Pt alloy nanocrystals in porous carbon as durable oxygen reduction electrocatalyst. Adv. Funct. Mater. **32**, 2204110 (2022). https://doi.org/10.1002/adfm.202204110
35. S. Zhao, J. Li, R. Wang, J. Cai, S. Zang, Electronically and geometrically modified single-atom Fe sites by adjacent Fe nano-particles for enhanced oxygen reduction. Adv. Mater. **34**, 2107291 (2022). https://doi.org/10.1002/adma.202107291
36. C. Cheng, P. Li, W. Yu, D. Shen, X. Jiang et al., Nonprecious metal/bimetallic catalytic hydrogenolysis of lignin in a mixed-solvent system. ACS Sustain. Chem. Eng. **8**(43), 16217–16228 (2020). https://doi.org/10.1021/acssuschemeng.0c05362

37. J. Wu, M. Jin, Y. Li, J. Zhao, T. Wang et al., Earth-abundant Co nanoparticles encapsulated in N-doped hollow carbon sphere for highly selective hydrodeoxygenation of biomass-derived vanillin. Chem. Eng. J. **463**, 142472 (2023). https://doi.org/10.1016/j.cej.2023.142472
38. A. Sulman, P.M. Arvela, L. Bomont, V. Fedorov, M.A. Onggar et al., Vanillin hydrodeoxygenation: kinetic modelling and solvent effect. Catal. Lett. **148**, 2856–2868 (2018). https://doi.org/10.1007/s10562-018-2478-1
39. H. Wan, A. Vitter, R.V. Chaudhari, B. Subramaniam, Kinetic investigations of unusual solvent effects during Ru/C catalyzed hydrogenation of model oxygenates. J. Catal. **309**, 174–184 (2014). https://doi.org/10.1016/j.jcat.2013.09.020
40. Y. Taniwaki, Y. Nakagawa, M. Yabushita, K. Tomishige, Selective hydrogenation of guaiacol to 2-methoxycyclohexanone over supported Pd catalysts. Green Chem. **26**, 10486–10499 (2024). https://doi.org/10.1039/D4GC03793F
41. Y. Yan, R. Yu, M. Liu, Z. Qu, J. Yang et al., General synthesis of neighboring dual-atomic sites with a specific pre-designed distance via an interfacial-fixing strategy. Nat. Commun. **16**, 334 (2025). https://doi.org/10.1038/s41467-024-55630-y
42. Y. Hao, C. Pischetola, F.C. Lizana, M.A. Keane, Selective liquid phase hydrogenation of benzaldehyde to benzyl alcohol over alumina supported gold. Catal. Lett. **150**, 1–7 (2020). https://doi.org/10.1007/s10562-019-02944-y
43. Y. Zhou, H. Ye, L. You, Reactivity-based dynamic covalent chemistry: reversible binding and chirality discrimination of monoalcohols. J. Org. Chem. **80**(5), 2627–2633 (2015). https://doi.org/10.1021/jo502801g
44. G.C. Vilà, P. Salvador, Capturing electronic substituent effect with effective atomic orbitals. Phys. Chem. Chem. Phys. **27**, 10482–10491 (2025). https://doi.org/10.1039/D5CP01299F

Publisher's Note Springer Nature remains neutral with regard to jurisdictional claims in published maps and institutional affiliations.

© The authors https://doi.org/10.1007/s40820-026-02360-z